Hierarchical carbon microflowers supported defect-rich Co$_3$S$_4$ nanoparticles: An efficient electrocatalyst for overall water splitting

Xiaojing Zhu [a, b], Jiale Dai [a], Ligui Li [a, b, c, *], Dengke Zhao [a], Zexing Wu [d], Zhenghua Tang [a], Li-Jun Ma [e], Shaowei Chen [a, f]

[a] New Energy Research Institute, School of Environment and Energy, South China University of Technology, Guangzhou, 510006, China
[b] Guangdong Provincial Key Laboratory of Petrochemical Pollution Process and Control, Guangdong University of Petrochemical Technology, Maoming, 525000, China
[c] The Key Lab of Pollution Control and Ecosystem Restoration in Industry Clusters, Ministry of Education, South China University of Technology, Guangzhou, 510641, China
[d] State Key Laboratory Base of Eco-chemical Engineering, College of Chemistry and Molecular Engineering, Qingdao University of Science & Technology, 53 Zhengzhou Road, Qingdao, 266042, China
[e] Key Laboratory of Theoretical Chemistry of Environment Ministry of Education, School of Chemistry and Environment, South China Normal University, Shipai, Guangzhou, 510631, China
[f] Department of Chemistry and Biochemistry, University of California, 1156 High Street, Santa Cruz, CA, 95064, USA

A B S T R A C T

Developing highly efficient and cost-effective bifunctional electrocatalysts for oxygen evolution reaction (OER) and hydrogen evolution reaction (HER) represents a judicious way to produce massive hydrogen fuel through electrochemical water splitting. Herein, defect-rich Co$_3$S$_4$ particles with a diameter less than 5 nm were in-situ grown on nitrogen-doped hierarchical carbon microflowers (Co$_3$S$_4$@FNC) through a simple hydrothermal method, in which an unconventional vulcanization process with the strongly coordinating ligand ethylenediamine and formaldehyde serving as structure-directive agents is resorted to effectively control the morphology of catalysts. The resultant Co$_3$S$_4$@FNC-Co3 comprises dense Co$_3$S$_4$ nanoparticles supported on ultrathin nitrogen-doped carbon nanosheets with a thickness of ca. 20 nm, as well as abundant defects on Co$_3$S$_4$ nanoparticles and highly porous textures on carbon microflowers. These nanostructure merits lead to efficient catalytic activities, featuring a small overpotential of only 250 mV and 140 mV for OER and HER electrocatalysis at 10 mV cm^{-2}. When Co$_3$S$_4$@FNC-Co3 is utilized as a bifunctional catalyst in an alkaline water electrolyzer, a bias of only 1.580 V is able to complement overall water splitting at 10 mA cm^{-2}. Results in present work may suggest a paradigm in the design and engineering of high-performance electrocatalysts based on nanocomposites of transition metal sulfides and carbons.

© 2019 Elsevier Ltd. All rights reserved.

1. Introduction

Challenges from energy crisis and environmental issues have triggered the rapid development of efficient and renewable energy technologies [1—6]. Among these, water splitting driven by electricity (e.g., alkali-electrolyzer) is a cost-effective and environmentally friendly technology for generating hydrogen from water, which has been regarded as a promising pathway towards hydrogen economy [7—13]. Yet, oxygen evolution reaction (OER) and hydrogen evolution reaction (HER), two half reactions of electrochemical water splitting process, are strongly influenced by the slow kinetics and large energy barriers, hence significantly reducing the overall efficiency of electrochemical water splitting [14,15]. It has been demonstrated that OER can be effectively catalyzed by Ru- and Ir-based noble metal nanomaterials, while HER can be efficiently catalyzed by Pt-based catalyst; however, their high costs and scarcity severely impede their widespread applications. Transition metal sulfides (TMSs) represent a class of emerging nonprecious metals-based electrocatalysts towards both OER and HER, and have been attracting significant attention because of their high intrinsic activity, cost-effectiveness, superb

electrical conductivity, and excellent anticorrosion performance in alkaline media [16—18]. Nevertheless, TMSs remain insufficiently explored, possibly because of the lack of suitable and viable preparation methods to maximize the exposure of the active sites [19,20].

Theoretically, minimizing the size of TMSs to a few nanometers (i.e. ultrafine nanoparticles) is considered as an effective strategy to maximize the utilization of metal centers (or generate more edge sites) [21], while concurrently constructing 3D architecture, for example, directly implanting the ultrafine TMSs nanoparticles onto conductive substrates (e.g., carbonaceous materials) or hybridizing them with conductive materials [22,23], should prevent them from restacking/aggregation and effectively reduce the length of ion and mass transport [24,25]. However, the corresponding synthetic route to this preferred 3D architecture usually involves multiple complicated steps, such as pre-synthesis of 3D carbonaceous substrate, high-temperature pyrolysis/carbonization, homogeneous deposition of metallic precursors onto substrate, sulfurization, etc. It is worth mentioning that alkaline-earth metal sulfides and thiourea (or thioacetamide) are usually employed as effective sulfurizing reagents to form metallic sulfides through ionic exchange reaction [26] and vulcanization process [14], respectively. However, these two conventional sulfurization methods usually encounter the challenge of size control in the synthesis of TMS-based electrocatalysts. For example, in case of using alkaline-earth metal sulfides as sulfurizing agents, the free S^{2-} ions can easily react with transition metal cations and form large aggregates, while in the case of using thiourea(TU) as the sulfurizing agent, the intermediate complex $[(NH_2)_2CS—M(OH^-)_2]$ can be decomposed to form metal sulfides (MS) by breaking the C—S bond [27]. The free MS can then easily nucleate and grow up into large aggregates due to the lack of any physical or chemical confinements. Therefore, novel vulcanization methods are highly desired.

Generally, ethylenediamine (En) can strongly chelate with M^{2+} to form soluble coordination complexes, $M(En)_2$ [28]. Hence, replacement of hydroxyl in $[(NH_2)_2CS—M(OH^-)_2]$ with En may lead to the formation of $[(NH_2)_2CS—M(En)_2]^{2+}$, which should impede the undesired reaction between M^{2+} and OH^- in a basic environment. Moreover, the strong coordination between M^{2+} and En in $[(NH_2)_2CS—M(En)_2]^{2+}$ should also slow down the nucleation of MS to yield small crystallites. Inspired by this idea, we speculate that when the $-NH_2$ groups in $[(NH_2)_2CS—M(En)_2]^{2+}$ are linked with more complicated chains, the corresponding physical and chemical

confinements to the nucleation and growth of TMSs should be more robust. This is the primary motivation of present work.

Herein, we describe an unconventional sulfurization strategy to the preparation of defect-rich ultrafine Co_3S_4 particles with a diameter size less than 5 nm (referred as sub-5 nm Co_3S_4 particles) supported on hierarchical carbon microflowers that are comprised with ultrathin carbon nanosheets via a simple hydrothermal process (Fig. 1a). Experimentally, TU, Co^{2+} and OH^- originated from the ionization of water coordinate to form intermediate complex $[(NH_2)_2CS—Co(OH^-)_2]$ [24]. Subsequently, the OH^- groups in the complex $[(NH_2)_2CS—Co(OH^-)_2]$ were substituted by strong chelating En ligands to form $[(NH_2)_2CS—Co(En)_2]^{2+}$, and then polymerized with CH_2O to afford TU-based oligomers through a Schiff-base coupling polymerization reaction (Fig. S1). The subsequent hydrothermal treatment caused further polymerization of the oligomers and concurrently carbonized to in-situ vulcanize metal atom centers. In this process, TU mainly serves as a carbon and sulfur source, while En and CH_2O act as a strong coordinating ligand and structure-directive reagent to control the morphology of the products, respectively. Hence, cobalt sulfide nanoparticles can be in-situ generated and homogeneously confined on carbon scaffold. Besides, thus-synthesized carbon substrate contains abundant oxygen-containing species, which enables a hydrophilic surface to facilitate mass diffusion [29]. Benefiting from the hierarchically porous structure in carbon microflower catalyst Co_3S_4@FNC (Fig. 1b), a high electrochemical surface area and sufficient exposure of active sites are realized, leading to low overpotentials of 250 and 140 mV for OER and HER electrocatalysis at a current density of 10 mA cm^{-2} in 1.0 M KOH, respectively. Moreover, an input bias of only 1.58 V is required to implement an overall water-splitting system with Co_3S_4@FNC-Co3 serving as both cathodic and anodic catalyst at a current of 10 mA cm^{-2}.

2. Experimental section

2.1. Synthesis of Co_3S_4@FNC nanocomposites

Co_3S_4@FNC composites were synthesized by a facile hydrothermal process. In a typical reaction, thiourea (TU) and Co(N-$O_3)_2\cdot6H_2O$ was dissolved in 40 mL of deionized water under magnetic stirring to form a uniform solution. Subsequently, ethylenediamine and formaldehyde (38 wt%) was added slowly into the above solution under stirring at room temperature for 24 h. The
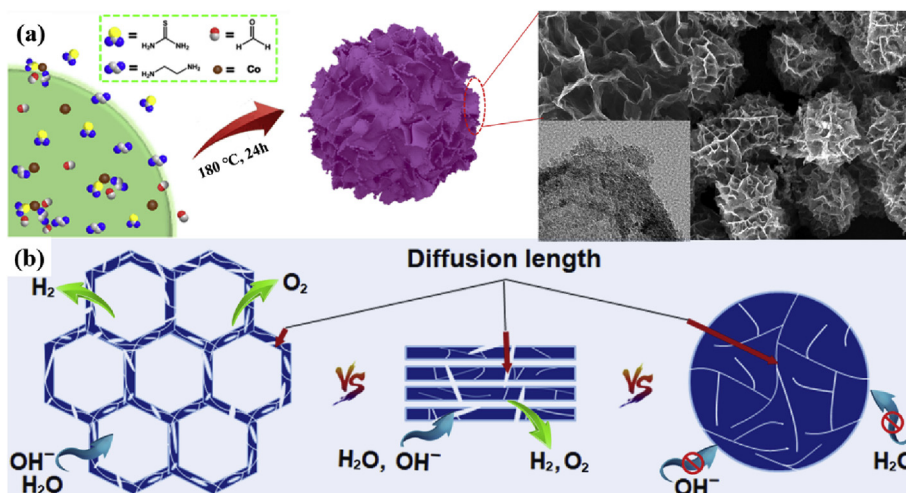

Fig. 1. Schematically illustrating (a) the fabrication process of Co_3S_4 hierarchical carbon microflowers; and (b) the advantages of hierarchical architecture for promoting electrolysis. (A colour version of this figure can be viewed online.)

final TU:Co:En:CH$_2$O molar ratio in the solution was 1.5:1:1:2. The obtained precursor solution was transferred into a stainless-steel Teflon-lined autoclave (50 mL) and subject to heat treatment in an oven at 180 °C for 24 h. The collected products were repeatedly washed with deionized water and ethanol for three times, and then dried at 60 °C for overnight. The final sample was denoted as Co$_3$S$_4$@FNC-Co3.

Additional samples were prepared in the same procedure except that the TU: Co(NO$_3$)$_2$·6H$_2$O molar ratio was altered to 3:1, 2:1 and 1:1, and the corresponding samples were referred to as Co$_3$S$_4$@FNC-Co1, Co$_3$S$_4$@FNC-Co2 and Co$_3$S$_4$@FNC-Co4, respectively.

A series of control samples were also prepared for comparison, with Co-TR referring to the sample synthesized without the addition of En and CH$_2$O, Co-TER for denoting the one without the addition of CH$_2$O, and Co-TFR for the one without adding En during synthesis.

2.2. Characterization

Scanning electron microscopy (SEM) measurements were conducted with a field-emission scanning electron micro-scope (ZEISS, Merlin). Transmission electron microscopic (TEM) measurements were conducted on a Tecnai G2-F20 equipped with an energy-dispersive X-ray spectrometer (EDS) detector at an applied voltage of 100 kV. For TEM measurement, a dispersion containing the catalysts was drop cast directly onto a copper grid coated with a holy carbon film. X-ray photoelectron Spectroscopy (XPS) measurements were performed on a Phi X-tool instrument. Powder XRD patterns were recorded with a Bruker D8-Advance diffractometer using Cu Kα radiation. Raman spectra were recorded from 100 to 2000 cm^{-1} on a RENISHAW in Via instrument with an Ar laser source of 488 nm in a macroscopic configuration. The Brunauer−Emmett−Teller (BET) surface area was determined by nitrogen adsorption and desorption at −196 °C using a Micromeritics ASAP 2010 instrument and the corresponding pore size distributions were calculated by using the Barrett−Joyner−Halenda (BJH) method. Electron paramagnetic resonance (EPR) spectra were recorded on a JEOL JES-FA200 spectrometer operated at 9.5 GHz under 100 K.

2.3. Electrochemical measurements

All electrochemical measurements were conducted on a CHI 750E electrochemical workstation (CH Instruments, Inc., China) using a conventional three-electrode cell in 1.0 M KOH at room temperature. For OER tests, a glassy carbon electrode (GCE) loaded with catalysts and an Ag/AgCl electrode (3 M KCl) were used as the working and reference electrode, respectively. As for the counter electrode, a platinum wire was used in OER measurement. Prior to electrochemical experiment, 2.0 mg of the as-prepared catalyst was dispersed in 980 μL of ethanol under ultrasonic agitation for 20 min. Subsequently, 20 μL of Nafion (5%) was added into the dispersion and further treated by sonication to form a homogeneous ink. Then, the catalyst ink was drop-cast onto the surface of the GCE at a catalyst loading of 0.404 mg cm^{-2} except for 0.2 mg cm^{-2} for commercial RuO$_2$. LSV scan rate: 10 mV s^{-1}.

HER measurements were carried out in 1.0 M KOH aqueous solutions a potential scan rate of 10 mV s^{-1}. An Ag/AgCl electrode and a carbon rod were used as the reference and counter electrode, respectively. The catalyst inks were fabricated in the same procedure and loading on carbon cloth (0.25 cm^2) was 0.4 mg cm^{-2}. Unless stated otherwise, all polarization curves conducted in a three-electrode configuration are corrected with iR compensation. The correction was conducted according to the following equation:

$$E_{compensated} = E_{measured} - iR_u$$

where $E_{compensated}$ is iR-corrected potential, $E_{measured}$ is experimentally measured potential, and R_u is the compensated resistance.

As for overall water splitting, the corresponding measurement was conducted using a two-electrode setup in 1.0 M KOH electrolyte. The scan rate for all polarization curves were 10 mV s^{-1} and the test voltage window was set at the range of 0.8−2.0 V. A carbon cloth (0.25 cm^2) loaded with 0.25 mg of catalyst was used as working electrode.

3. Results and discussion

As shown in Fig. 1a, the Co$_3$S$_4$@FNC nanocomposites with hierarchical structure were facilely prepared by a hydrothermal process, in which Co^{2+} ions were used as the metal source, and the polymer matrix of TU-En-CH$_2$O was employed as the carbonaceous scaffold, chelating and sulfurizing agent. Hydrothermal processing led to the formation of 3D flower-like nitrogen-doped carbon (FNC) structures with hierarchical pores for promoting mass diffusion, and on which ultrafine Co$_3$S$_4$ nanoparticles were in-situ grown.

To determine the optimum conditions for the formation of the hierarchical microflowers, different feed ratios of TU:Co:En:CH$_2$O were examined (for more details see Figs. S2−5 in the Supplementary Information). Based on the series catalytic results depicted below, Co$_3$S$_4$@FNC-Co3 synthesized at a TU:Co:En:CH$_2$O feed ratio of 1.5:1:1:2 was found to be the optimal sample. The SEM image in Fig. 2a showed a 3D flower-like morphology with a diameter of 5−10 μm. From the enlarged SEM image (Fig. 2b), one can see that the microflower morphology possesses abundant submicron open-channel cavities consisting of interconnected nanosheets with a thickness of about 20 nm. In fact, high-angle annular dark-field scanning TEM (HAADF-STEM) studies (Fig. 2c−d) clearly show the formation of a flower-like structure, with interconnected nanosheets of 16−20 nm in thickness, and a rough surface with numbers of nanoparticles could be resolved for these interconnected nanosheets (Fig. S6). The magnified TEM image (Fig. 2e) shows that the nanosheets contain large number of ultrafine nanoparticles with a predominant size of ~4 nm. From the high-resolution TEM image (Fig. 2f), one can see lattice fringes with a d-spacing of 0.284 nm, corresponding to the (311) lattice planes of orthorhombic phase Co$_3$S$_4$. Furthermore, discontinuous lattice fringes (see the dark patch regions denoted by yellow circles) are also observed, suggesting the existence of defects in Co$_3$S$_4$ crystallites. Statistical analysis based on more than 100 nanoparticles suggested that the Co$_3$S$_4$ nanoparticles were mostly 4.4 nm in diameter, as manifested in the core-size histogram in Fig. 2g. From the SAED patterns depicted in Fig. 2h, diffraction rings with a d-spacing of 0.285 nm and 0.181 nm were resolved, corresponding to the spacings of the (311) and (511) planes, respectively, again indicative of the formation of ultrafine Co$_3$S$_4$ nanoparticles. Besides, elemental mapping measurements (Fig. 2i) showed that the C, N, O, S and Co elements were homogeneously distributed on Co$_3$S$_4$@FNC-Co3 and the S/Co ratio determined by EDS measurement was 1.35 (Fig. S7), which was consistent with the stoichiometric ratio of Co$_3$S$_4$. Besides, selected-area elemental mapping images confirmed the uniformly distributed C, S and Co elements on Co$_3$S$_4$@FNC-Co3 (Fig. S8). These observations reveal that the TU-Co^{2+}-En route can indeed effectively impede the excessive growth of metal sulfide particle and hence facilitate the formation of ultrafine Co$_3$S$_4$ nanoparticles on the interconnected nanosheets of 3D carbon microflowers. Furthermore, the crystalline structures of the composites were examined by X-ray diffraction (XRD) measurements. As shown in Fig. 2j, the Co$_3$S$_4$@FNC-Co3 sample displayed a series of diffraction peaks at 2θ = 31.2°, 38.5°, 47.5°, 50.2° and 55.1°, which were
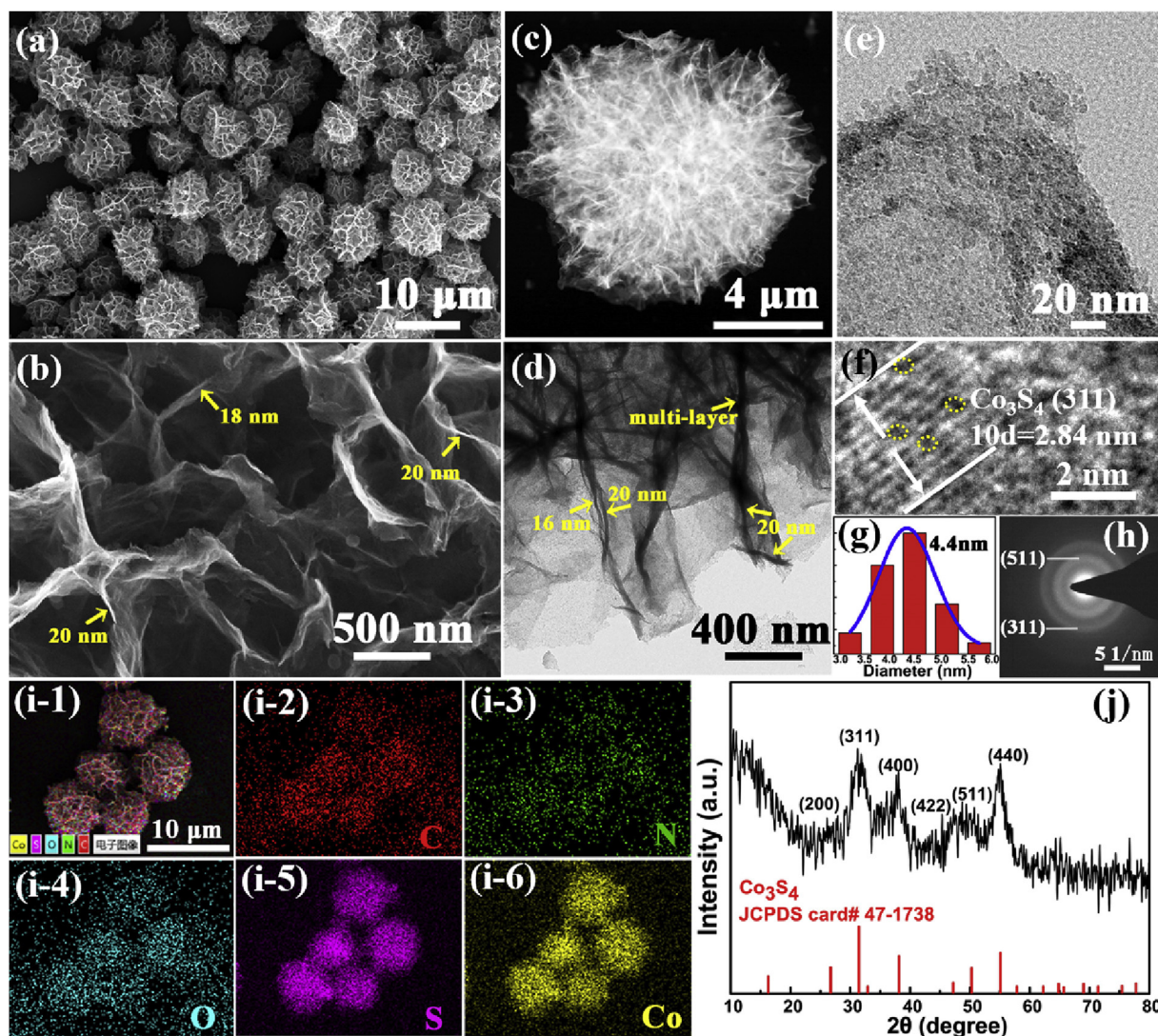
Fig. 2. (a) Representative SEM image; (b) Enlarged SEM image; (c) HADDF-STEM image; (d, e) TEM images with different magnifications; (f) HR-TEM image; (g) the core-size histogram; (h) SAED image; (i-1) overlap of elemental maps of C, N, O, S, and Co; and the corresponding elemental map of (i−2) C, (i-3) N, (i-4) O, (i-5) S, and (i-6) Co, and (j) XRD pat-terns of Co_3S_4@FNC-Co3. (A colour version of this figure can be viewed online.)

assigned to the (311), (400), (422), (511), and (440) planes of crystalline Co_3S_4 (JSPDS Card# 47−1738), respectively. In Raman measurements, the strong peak at 666 cm^{-1} (Fig. S9) is correlated to the vibration of Co−S bond [30], whereas the G band, a peak that usually appears at about 1500 cm^{-1} for graphitic carbon, is hardly resolved, signifying a low graphitization degree for the hierarchical carbon microflowers. However, the above observations confirm the formation of hierarchical carbon microflowers comprised with defect-rich sub-5 nm Co_3S_4 particles and ultrathin carbon nanosheets via a simple hydrothermal method.

The chemical composition and valence state of the Co_3S_4@FNC-Co3 sample were then determined by X-ray photoelectron spectroscopy (XPS) measurements. As shown in Fig. 3a, The C (57.53 at %), N (6.41 at%), O (18.39 at%), S (10.15 at%) and Co (7.52 at%) elements can be readily resolved and the molar ratio of S/Co is calculated to be 1.35, as listed in Table S1, which coincides with the stoichiometric ratio of Co_3S_4. Deconvolution of the C 1s scan of Co_3S_4@FNC-Co3 (Fig. 3b) yields five peaks, which are attributed to the sp2-hybridized C (284.6 eV) of graphite, sp3-hybridized C (285.1 eV), C−N species (285.8 eV) as well as the C−O (286.6 eV)

and C═O moieties (288.1 eV), respectively. The high-resolution XPS spectrum of Co 2p can be deconvoluted into three pairs of obvious peaks in Fig. 3c, where the peaks centered at 780.4 and 798.8 eV are attributed to Co^{2+},while the peaks at 778.7 and 793.8 eV are from Co^{3+}, as well as a pair of satellite peaks observed at 784.2 and 803.7 eV [31]. Based on the integrated peak areas, the molar ratio of Co^{2+}/Co^{3+} is determined to be about 0.80, which is obviously higher than that of Co_3S_4@FNC-Co4 (0.54) but smaller than those of Co_3S_4@FNC-Co1 (1.11) and Co_3S_4@FNC-Co2 (0.91) in Figs. S10a−c. One can find that the molar ratio of Co^{2+}/Co^{3+} increases with increasing the molar ratio of TU/Co (Fig. S10d), probably due to the reason that the presence of excessive TU facilitates the formation of defects [32], i.e. abundant sulfur vacancies in present work [33,34]. As for the deconvolution fitting of the S 2p XPS spectrum (Fig. 3d), four well-resolved peaks are observed. The doublets at 161.5 and 163.2 eV are attributed to the S 2p3/2 and S 2p1/2, respectively [35]. In addition, the peak at 163.8 eV is a typical peak of Co−S species, and the peak appears at 162.4 eV is attributed to the presence of S^{2-} ions in a low coordination state on surface, while the peak at about 168.7 eV is ascribed to the shakeup satellite peak [36]. The
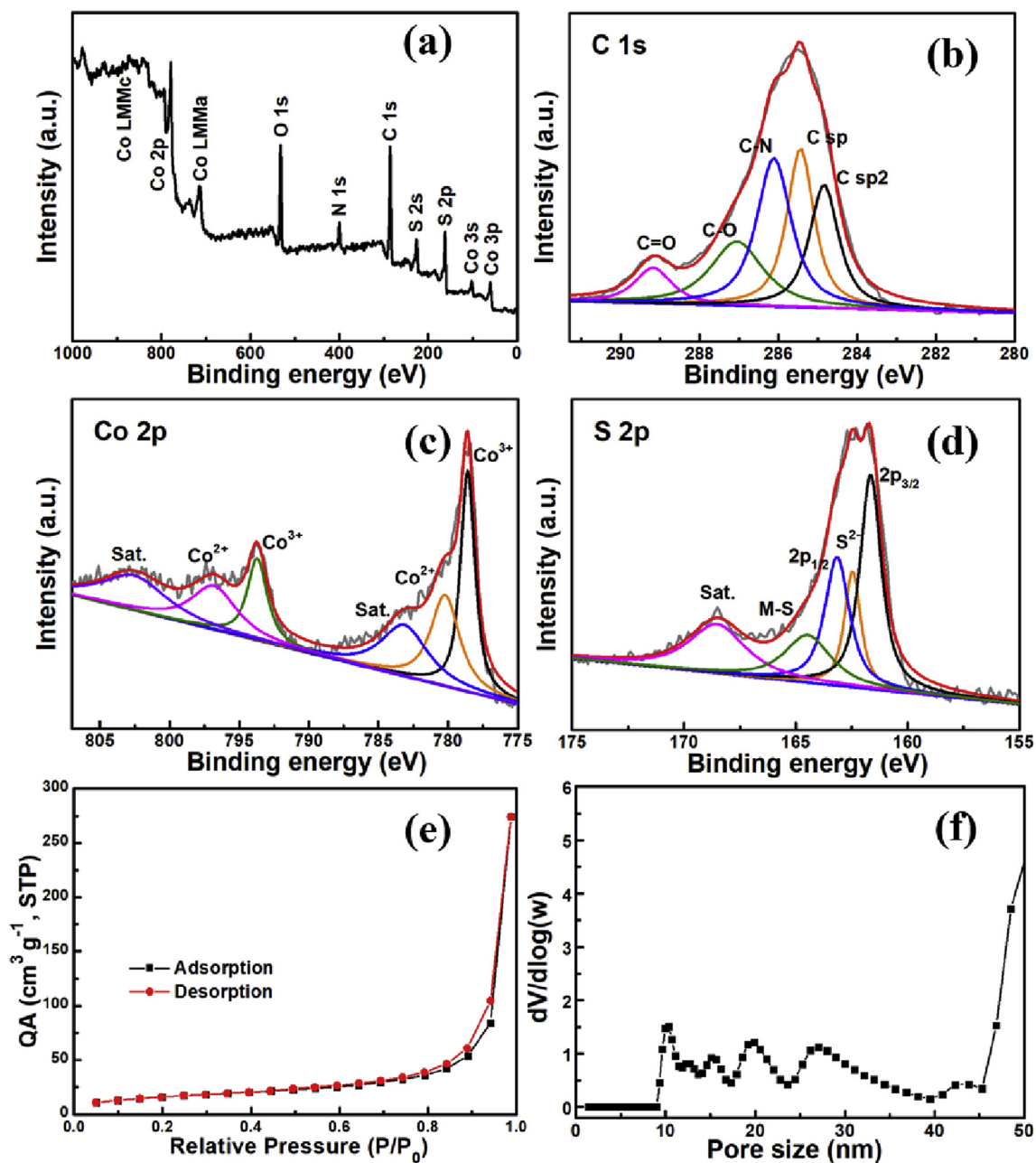
Fig. 3. (a) XPS survey spectrum; and high-resolution scans of (b) C 1s, (c) Co 2p and (d) S 2p electrons for Co_3S_4@FNC-Co3. (e) N_2 adsorption/desorption isotherm, and (f) the corresponding pore size distribution of Co_3S_4@FNC-Co3. (A colour version of this figure can be viewed online.)

observations of a high ratio of Co^{2+} to Co^{3+} and the fingerprint peak of low-coordination S atoms in S 2p1/2 XPS spectrum suggest the existence of sulfur vacancies in Co_3S_4 nanoparticles supported on the hierarchical carbon microflowers [37,38], which is in good agreement with TEM and SAED results. Additionally, the high-resolution O 1s spectrum (Fig. S11a) of the Co_3S_4@FNC-Co3 sample can be fitted with three intensive peaks located at 531.8, 532.5 and 533.8eV, respectively, which are attributed to the C=O and C−O−C, and C−OH moieties [24], without the observation of metal oxide species. The corresponding N 1s spectrum is shown in Fig. S11b, where a strong peak located at 400.1 eV is ascribed to the pyrrole-N in the matrix of carbon microflowers.

Electron paramagnetic resonance (EPR) measurement was also conducted for the Co_3S_4@FNC composites. As show in Fig. S12, an

obvious EPR resonance signal with g = 2.002 can be observed in Co_3S_4@FNC composites expect for Co_3S_4@FNC-Co4 sample. The emergence of strong EPR signal at g-value of 2.002 is due to the presence of sulfur vacancies. One can find that the content of defect decreases with decreasing molar ratio of TU/Co.

BET measurements were then conducted to determine the specific surface area and porous structure of the nanocomposites. As shown in Fig. 3e, the N_2 adsorption amount abruptly increases at a higher relative pressure ($P/P_0 > 0.95$) and the adsorption-desorption isotherm displays a clear hysteresis loop, indicative of the coexistence of meso- and macropore pores in the Co_3S_4@FNC composites [39—41]. This conclusion is supported by the corresponding pore size distribution depicted in Fig. 3f, where the pore diameter varies from 10.0 nm to tens of nanometers, with an

obviously hierarchical porosity. The specific surface area (S_{BET}) is calculated to be 77 m^2 g^{-1} for Co$_3$S$_4$@FNC-Co1, 64 m^2 g^{-1} for Co$_3$S$_4$@FNC-Co2, 59 m^2 g^{-1} for Co$_3$S$_4$@FNC-Co3 and 30 m^2 g^{-1} for Co$_3$S$_4$@FNC-Co4 (Fig. S13). These results show that the BET surface area of Co$_3$S$_4$@FNC-Co samples continuously decreases with increasing the feeding amount of cobalt salt during synthesis. Additionally, the large specific surface area along with the abundant hierarchical pores in Co$_3$S$_4$@FNC-Co3 may provide highly accessible active sites, and enable fast mass transfer, which are beneficial to efficient electrocatalysis [42]. The content of Co element quantitatively determined by thermogravimetric analysis (TGA) in air (Fig. S14) is 27.2 wt% for Co$_3$S$_4$@FNC-Co1, 32.5 wt% for Co$_3$S$_4$@FNC-Co2, 38.9 wt% for Co$_3$S$_4$@FNC-Co3, and 46.0 wt% for Co$_3$S$_4$@FNC-Co4.

In order to investigate the function of each component and possible growth mechanism of the 3D flower-like microstructure, a series of control samples were also prepared for comparison, including Co-TR that was synthesized without the addition of En and CH$_2$O, Co-TER that was synthesized without the addition of CH$_2$O, and Co-TFR that was prepared without the addition of En during synthesis. It is found that, without the addition of En and CH$_2$O, polyhedron-like clusters comprised with multiple thick twinning plates are observed, instead of the ultrathin nanosheets (Fig. 4a and b). When only En was added into the system, the resultant Co-TER showed a hollow sphere structure with a wall thickness of about 200 nm (Fig. 4c and d), indicating that En serves as a spherical structure-directive agent. Differently, in the presence

of only CH$_2$O, the resultant Co-TFR product was comprised with a large number of rough nanosheets (Fig. 4e and f), implying that CH$_2$O likely acted as a 2D growth-guiding agent. As a consequence, various architecture of the resultant, such as 0D hollow sphere and 2D nanosheet, can be selectively prepared by tuning the addition ratio of En:CH$_2$O in hydrothermal synthesis. However, after delicately controlling the cooperation effect of these two functional agents by optimizing the ratio of En:CH$_2$O, 3D carbonaceous microflowers comprised with ultrathin nanosheets are obtained, as shown in Fig. 2a. Additionally, it is worth mentioning that, a non-stoichiometric cobalt sulfide CoS$_{1.097}$ (PDF#19−0366) that is different from those observed in Co-TER, Co-TFR and Co$_3$S$_4$@FNC-Co3 samples, was observed in the XRD pattern of Co-TR (Fig. S15), further confirming that the involved mechanism in preparation of cobalt sulfide by using thiourea as sulfur precursor is different from that in the conventional hydrolysis-deposition process.

Fig. 5a illustrates the linear polarization curves of different catalysts with potentials sweeping from +1.00 to +1.80 V, where a sudden increase of voltammetric currents was observed for all catalysts, signifying an apparent OER electrocatalytic activity. Impressively, the Co$_3$S$_4$@FNC-Co3 sample exhibits an obviously enhanced performance with an overpotential (η_{10}) of only 250 mV to reach 10 mA cm^{-2}, much lower than the 330, 380 and 530 mV observed for Co-TFR, Co-TER and Co-TR samples, respectively. The higher OER catalytic activities for Co$_3$S$_4$@FNC-Co3 may derive from its larger specific surface area (Fig. S16a), as compared with the other three samples in the series. Interestingly, Co$_3$S$_4$@FNC-Co3
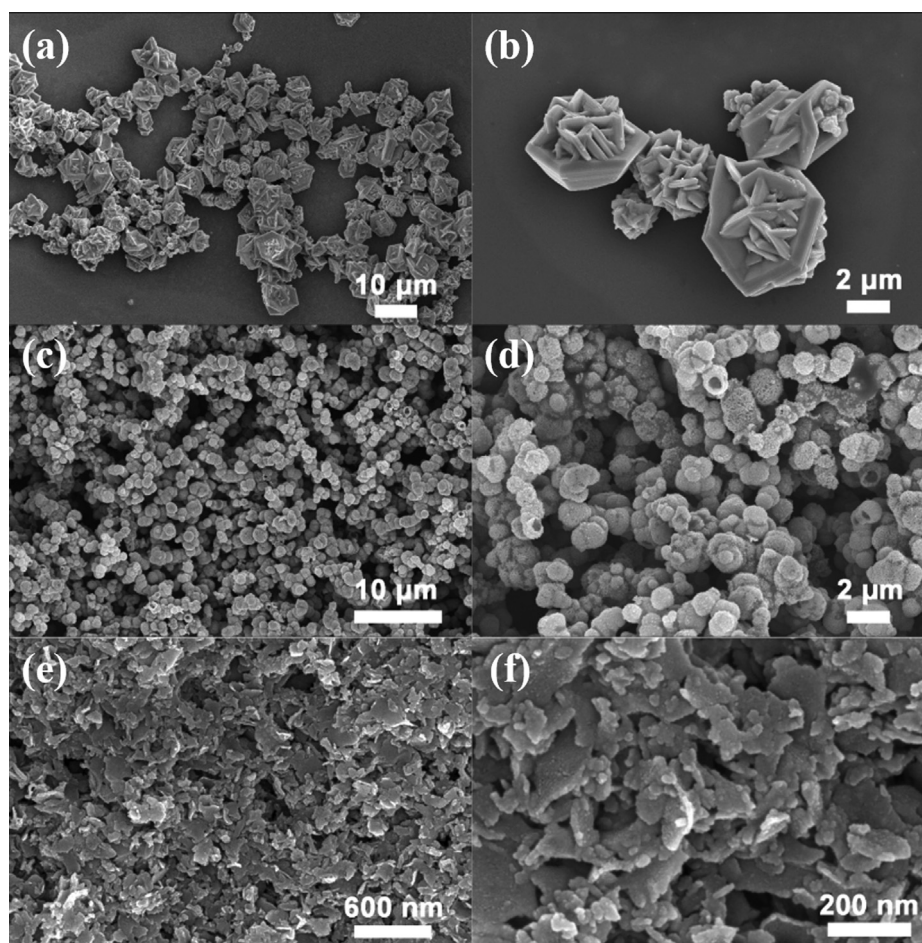

Fig. 4. SEM images of different samples: (a, b) Co-TR, (c, d) Co-TER, and (e, d) Co-TFR. (A colour version of this figure can be viewed online.)
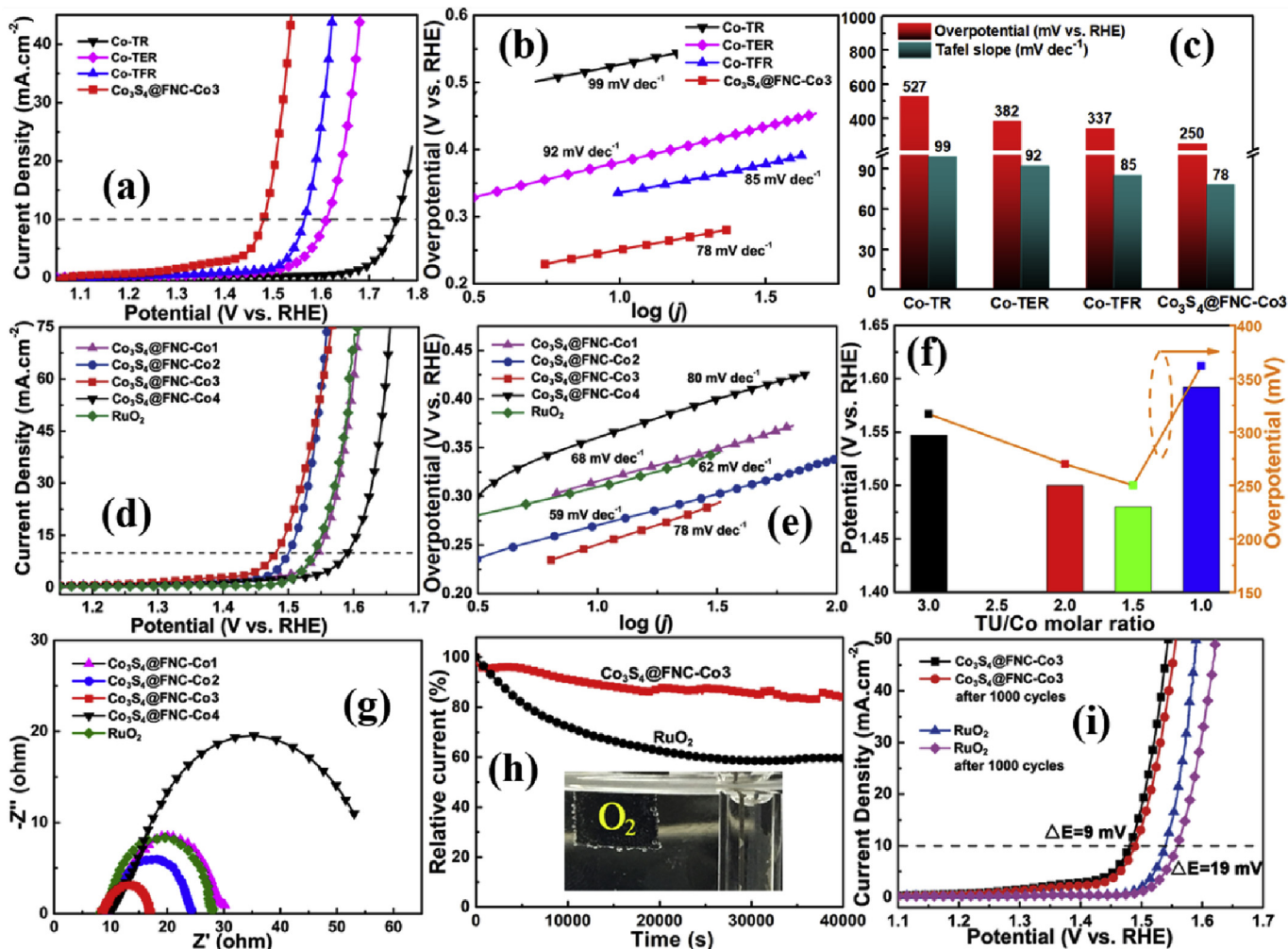
Fig. 5. (a) LSV curves for OER; (b) Tafel plots; and (c) Histogram showing the $E_{OER, 10}$ and Tafel plots of different electrocatalysts, (d) LSV curves of commercial RuO_2 and Co_3S_4@FNC composites prepared at different TU/Co molar ratios in 1.0 M KOH, (e) Tafel plots of different OER catalysts, (f) Histogram showing the $E_{OER, 10}$ of the Co_3S_4@FNC electrocatalysts and the plot showing the variation of η_{10}, (g) Electrochemical impedance spectra of different catalysts deposited on a GCE electrode at +1.56 V for OER conducted in 1.0 M KOH aqueous solution with an AC amplitude of 5 mV within the frequency range of 100 kHz to 0.01 Hz, (h) Chronoamperometric plots for comparing the operation stability of Co_3S_4@FNC-Co3 and RuO_2 catalyst at the applied potential of +1.50 V and +1.55 V (vs. RHE), respectively. (i) LSV curves of Co_3S_4@FNC-Co3 and RuO_2 before and after 1000 cycles of ADT test. All the potentials are referred to reversible hydrogen electrode (RHE) and have been corrected by iR compensation. Inset to panel (h) is the photograph showing the generation of oxygen bubbles on Co_3S_4@FNC-Co3 during chronoamperometric OER measurement. (A colour version of this figure can be viewed online.)

also shows a higher current density than the other three samples in the series at the same potential after normalizing with the BET specific surface area (Fig. S16b), which suggests the presence of a higher density of OER catalytically active species on Co_3S_4@FNC-Co3 than other samples in the series. In the corresponding Tafel plots shown in Fig. 5b, the Tafel slope of Co_3S_4@FNC-Co3 is estimated to be 78 mV dec^{-1}, which is considerably lower than that of Co-TFR (85 mV dec^{-1}), Co-TER (92 mV dec^{-1}), and Co-TR (99 mV dec^{-1}), further confirming the fast OER kinetics for Co_3S_4@FNC-Co3 catalyst. The key parameters for these four samples in OER catalysis are then summarized in Fig. 5c for comparison. In addition, the charge transfer resistant (R_{CT}) and electrochemical surface area (ECSA) were further analyzed to shed light on the fast OER catalytic kinetics of Co_3S_4@FNC-Co3. The corresponding electrochemical impedance spectra (EIS) depicted in Fig. S17 suggest that Co_3S_4@FNC-Co3 displays a charge transfer resistance much lower than Co-TR, Co-TER and Co-TFR catalysts in alkaline electrolyte, which may facilitate electron transport and eventually enhance the kinetics of OER electrocatalysis on Co_3S_4@FNC-Co3. The corresponding ECSAs of these catalysts were evaluated by calculating the

electrochemical double-layer capacitance (C_{dl}) from the cyclic voltammetry curves acquired at different scan rates. As shown in Figs. S18 and S19, a C_{dl} value of 18.6 mF cm^{-2} is determined for Co_3S_4@FNC-Co3, which is also much higher than Co-TR (2.8 mF cm^{-2}), Co-TER (8.3 mF cm^{-2}), and Co-TFR (11.0 mF cm^{-2}) in 1.0 M KOH aqueous electrolyte. Based on these results, one can conclude that the Co_3S_4@FNC-Co3 catalyst indeed has a much larger ECSA to effectively expose the electrocatalytically active sites for OER.

Besides, the OER activity of the series of Co_3S_4@FNC composites synthesized at different TU/Co molar ratio was also investigated. As shown in Fig. 5d, the potential ($E_{OER,10}$) required to reach a current density of 10 mA cm^{-2} was determined to be +1.480 V for Co_3S_4@FNC-Co3, much lower than +1.547 V for Co_3S_4@FNC-Co1, +1.500 V for Co_3S_4@FNC-Co2, and +1.591 V for Co_3S_4@FNC-Co4. Actually, the activity of Co_3S_4@FNC-Co3 is even better than that of the benchmark RuO_2 catalyst (+1.540 V, Fig. 5d and f), and superior to many nonprecious metal compounds based electrocatalysts reported in literature (Table S2). Impressively, even the loading of commercial RuO_2 catalyst is the same as Co_3S_4@FNC

composites, the OER catalytic activity of Co$_3$S$_4$@FNC-Co3 is still superior to commercial RuO$_2$ catalyst (Fig. S20), suggesting the high potential application of Co$_3$S$_4$@FNC-Co3 as efficient electrocatalyst for OER. As for the corresponding Tafel plots depicted in Fig. 5e, all the Co$_3$S$_4$@FNC samples show a Tafel slope close to that of commercial RuO$_2$ catalyst (62 mV dec^{-1}), with 68 mV dec^{-1} for Co$_3$S$_4$@FNC-Co1, 59 mV dec^{-1} for Co$_3$S$_4$@FNC-Co2, 78 mV dec^{-1} for Co$_3$S$_4$@FNC-Co3 and 80 mV dec^{-1} for Co$_3$S$_4$@FNC-Co4. These results suggest fast electron transfer kinetics and strong bubble-releasing ability for the series of Co$_3$S$_4$@FNC samples. For the electrochemical impedance spectra (EIS) in Fig. 5g, the Nyqusit plots reveal that the charge transfer resistance of Co$_3$S$_4$@FNC-Co3 is obviously smaller than RuO$_2$ and other Co$_3$S$_4$@FNC composites, indicating that Co$_3$S$_4$@FNC-Co3 possesses the fastest charge transfer kinetics among all the investigated samples.

Chronoamperometric measurements further confirm the presence of remarkable stability for Co$_3$S$_4$@FNC-Co3, as compared with commercial RuO$_2$ catalyst. From Fig. 5h, one can see that the current of the RuO$_2$-modified electrode gradually decreases to about 60.0% of its initial value after continuous operation for 40,000 s, while a much higher retention of 87.0% is observed for Co$_3$S$_4$@FNC-Co3. Meanwhile, oxygen bubbles are clearly observed to generate on Co$_3$S$_4$@FNC-Co3 surface during OER chronoamperometric measurement (inset to Fig. 5f). The multi-step chronopotentiometry was also resorted to assess the electrochemical performance of Co$_3$S$_4$@FNC-Co3 in a current density ranging from 10 mA cm^{-2} to 400 mA cm^{-2}. As shown in Fig. S22, upon stepwise increasing in the current density, the required potential for Co$_3$S$_4$@FNC-Co3 modified electrode increases accordingly but stabilizes quickly, indicative of outstanding mass transfer property and mechanical robustness of Co$_3$S$_4$@FNC-Co3 based electrode. Moreover, the operation stability of the electrocatalysts was evaluated by accelerated durability test (ADT), in which Co$_3$S$_4$@FNC-Co3 only displayed a slight reduction (a positive potential shift of 9 mV) in

the OER current after 1000 cycles in 1.0 M KOH, while considerable OER current degradation (19 mV) was observed for RuO$_2$ (Fig. 5i), again signifying that the operation stability for Co$_3$S$_4$@FNC-Co3 is superior to that of RuO$_2$. After the above long-time OER testing, Co$_3$S$_4$@FNC-Co3 largely retained its flower-like morphology, although a slight aggregation and collapse was observed, indicative of its excellent structural stability (Fig. S23a). XRD measurements reveal the emergence of Co(OH)$_2$ and CoOOH in Co$_3$S$_4$@FNC-Co3 (Fig. S23b), indicating that Co$_3$S$_4$ was partially transformed to Co(OH)$_2$ and CoOOH after prolonged operation in alkaline electrolytes. In addition, from the XPS spectra in Fig. S23c, it can be found that the binding energies of Co 2p peaks are obviously shifted to higher values. Meanwhile, the two peaks at 780.2 and 783.5 eV become more evident after long-time OER measurements, which could be ascribed to the CoOOH [43,44] and Co(OH)$_2$ phases, respectively [45,46]. Moreover, the intensity of the S 2p peak is significantly reduced (Fig. S23d), indicating that S element was severely leached during continuous OER measurement. Similarly, the deconvoluted O 1s spectrum showed Co—O components (Fig. S23e), which is likely caused by the in-situ electrochemical oxidation of Co$_3$S$_4$ surface during the long-term water oxidation process. These results unambiguously demonstrate that after the long-term water oxidation process, Co$_3$S$_4$ was obviously converted to Co (oxy) hydroxide that actually serve as the catalytically active species for OER [47,48].

The Co$_3$S$_4$@FNC-Co3 sample also shows considerable catalytic activities toward HER in alkaline electrolyte (1.0 M KOH solution). Fig. 6a depicts the HER LSV curves for the series of Co$_3$S$_4$@FNC-Co composites and commercial Pt/C (20 wt%) catalyst, where one can find that Co$_3$S$_4$@FNC-Co3 hybrid exhibits a high HER activity, featuring a small over potential of 140 mV at a current density of 10 mV cm^{-2}, obviously lower than Co$_3$S$_4$@FNC-Co1 (258 mV), Co$_3$S$_4$@FNC-Co2 (176 mV), Co$_3$S$_4$@FNC-Co4 (296 mV), and comparable to or even better than most leading metal sulfide-based
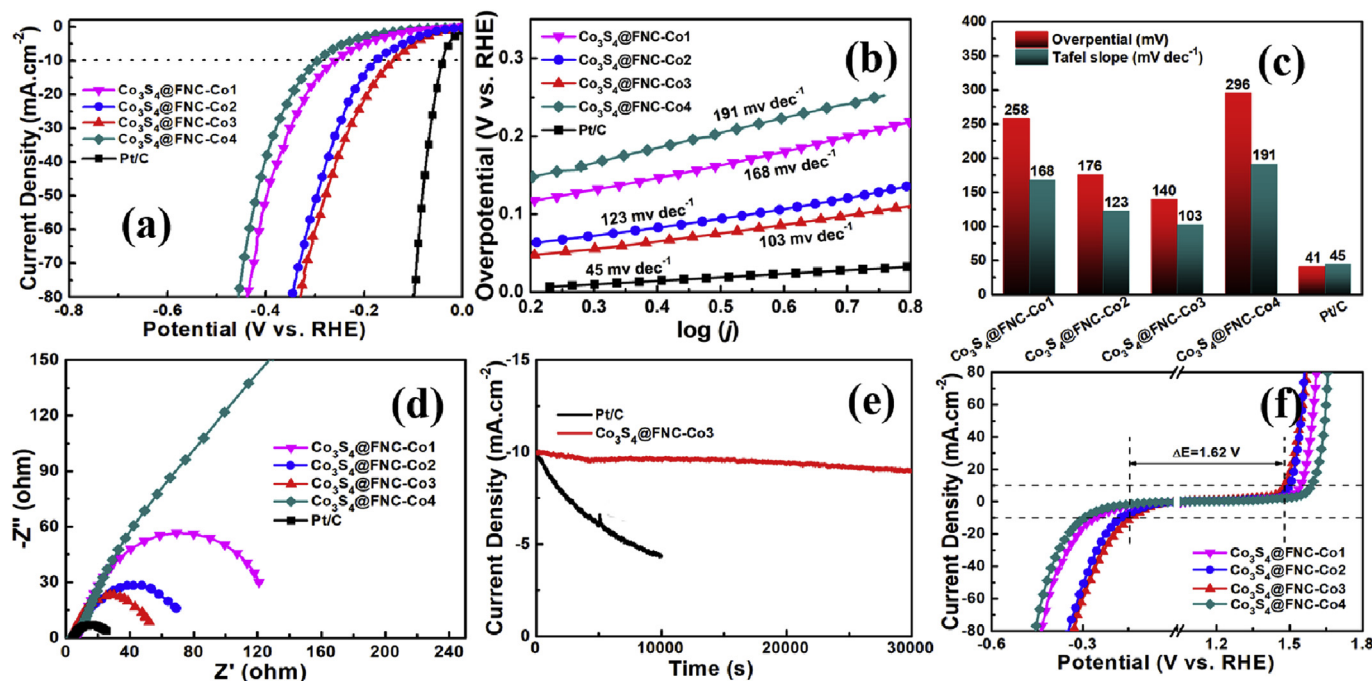

Fig. 6. (a) polarization curves for HER and (b) the corresponding Tafel plots of different electrocatalysts in 1.0 M KOH solution. (c) comparison of overpotentials and Tafel slopes for the different samples. (d) Electrochemical impedance spectra of different catalysts deposited on a GCE electrode at −0.20 V for HER conducted in 1.0 M KOH aqueous solution with an AC amplitude of 5 mV within the frequency range of 100 kHz to 0.01 Hz. (e) Long-term stability of Pt/C and Co$_3$S$_4$@FNC-Co3 at the applied potential of −140 mV and −41 mV (vs. RHE), respectively. (f) Combined OER and HER catalytic behavior of Co$_3$S$_4$@FNC composites. (A colour version of this figure can be viewed online.)

catalysts recently reported in alkaline media (Table S3). These findings indicated that Co$_3$S$_4$@FNC-Co3 possessed high HER activity, mainly attributed to the presence of a large specific surface area and a high density of highly active Co$_3$S$_4$ nanoparticles. The Co$_3$S$_4$@FNC-Co3 also exhibited a smaller Tafel slope of 103 mV dec^{-1}, as compared with Co$_3$S$_4$@FNC-Co1 (168 mV dec^{-1}), Co$_3$S$_4$@FNC-Co2 (123 mV dec^{-1}), and Co$_3$S$_4$@FNC-Co4 (191 mV dec^{-1}) in the linear region (Fig. 6b), which suggests a fast H$_2$ generation reaction kinetics with a combined Volmer—Heyrovsky mechanism for Co$_3$S$_4$@FNC-Co3 catalyst. The corresponding results of comparison studies on the over potential and Tafel slopes for these Co$_3$S$_4$@FNC-Co samples and Pt/C catalyst are summarized in a histogram displayed in Fig. 6c. The exchange current density (j_0) is also a kinetic parameter to evaluate the intrinsic HER catalytic activity of a sample, and the j_0 value can be obtained by extrapolating the Tafel plot to an overpotential of 0 V (Fig. S24 and Table 1). One can find that Co$_3$S$_4$@FNC-Co3 exhibits the highest j_0 value among these Co$_3$S$_4$@FNC composites, indicating that Co$_3$S$_4$@FNC-Co3 has the fastest electron-transfer rate in the series. The TOF for HER on Co$_3$S$_4$@FNC-Co3 is calculated to be 4.13 $\times$ 10^{-2} s^{-1} at η = 200 mV (Fig. S25 and Table 1). Besides, the electrochemical impedance spectra (EIS) in Fig. 6d, which revealed that the Co$_3$S$_4$@FNC-Co3 sample delivered the smallest charge transfer resistance (R_{CT}) among the series of Co$_3$S$_4$@FNC-Co composite catalysts, again signifying the presence of a rapid electron transport process in hydrogen evolution on Co$_3$S$_4$@FNC-Co3. Electrocatalytic stability of Co$_3$S$_4$@FNC-Co3 was then evaluated by chronoamperometric measurements in 1.0 M KOH aqueous solution. As illustrated in Fig. 6e, the Co$_3$S$_4$@FNC-Co3 catalyst could retain 92.4% of its initial current density after continuously catalyzing HER for 30000 s, while a much lower retention value of 54.8% was observed for Pt/C electrode after continuously working for only 10000 s, clearly demonstrating a higher working durability for Co$_3$S$_4$@FNC-Co3 than state-of-the-art Pt/C catalyst. Faradaic efficiency (FE) is usually used to evaluate the charge transfer efficiency of catalyst in electrolysis, which is calculated to be 99.0% for Co$_3$S$_4$@FNC-Co3 by comparing the theoretical and experimental amounts of produced H$_2$ (Fig. S26).

The OER and HER electrocatalysis of Co$_3$S$_4$@FNC composites are also conducted in 0.1 M KOH and 0.5 M H$_2$SO$_4$ aqueous solutions (Fig. S21), and the corresponding results suggest that the overall OER and HER electrocatalysis activities of present Co$_3$S$_4$@FNC composites are more efficient in 1.0 M KOH aqueous solution than those observed in 0.1 M KOH and 0.5 M H$_2$SO$_4$ aqueous solutions.

Moreover, Co$_3$S$_4$@FNC-Co3 can also largely retain its microflower-like morphology during electrocatalysis, as evidenced by the SEM images taken after continuously catalyzing HER for 30000 s (Fig. S27a). From the corresponding XRD profile determined after long-term HER catalysis, besides Co$_3$S$_4$ phase, a new crystalline phase Co(OH)$_2$ was also detected (Fig. S27b), implying partial Co$_3$S$_4$ was transformed to Co(OH)$_2$ after long-time HER testing. Similarly, Co(OH)$_2$ species is resolved in the Co 2p and O 1s

HR-XPS peaks (Figs. S27c and e) for Co$_3$S$_4$@FNC-Co3 after continuously catalyzing HER for 30000 s [43]. However, as mentioned above, although partial Co$_3$S$_4$ was transformed to Co(OH)$_2$, Co$_3$S$_4$@FNC-Co3 was able to maintain 92.4% of its catalytic current after 30000 s, indicating a high HER stability for Co$_3$S$_4$@FNC-Co3. Furthermore, the combined HER and OER behaviors of the electrocatalysts were also provided to better evaluate the bifunctional catalytic activities of Co$_3$S$_4$@FNC composites toward OER and HER. As illustrated in Fig. 6f, Co$_3$S$_4$@FNC-Co3 displays a much smaller potential gap of 1.62 V ($\Delta E = E_{j=10, OER} - E_{j=10, HER}$) than the other investigated Co$_3$S$_4$@FNC composites, confirming a high bifunctional catalytic activity towards HER and OER for Co$_3$S$_4$@FNC-Co3. When normalized with electrochemical surface area (ECSA) (Figs. S28—30) or mass (Fig. S31), Co$_3$S$_4$@FNC-Co3 still shows the highest OER and HER specific activities among the series, signifying the high intrinsic catalytic activities of Co$_3$S$_4$@FNC-Co3.

Encouraged by the above promising half-cell electrocatalysis performance toward OER and HER in 1.0 M KOH electrolyte, the Co$_3$S$_4$@FNC-Co3 was utilized as a bifunctional catalyst for overall water splitting. As depicted in Fig. 7a, a bias of only 1.580 V was required to realize a water-splitting current density of 10 mA cm^{-2} by using carbon cloth based electrodes loaded with 1 mg cm^{-2} of Co$_3$S$_4$@FNC-Co3, which is comparable or even superior to the leading nonprecious metal or metal chalcogenides based electrocatalysts recently reported in literature for overall water splitting, such as Co$_3$S$_4$@MoS$_2$ (1.58V) [49], Ni@NC800 (1.60 V) [50], Co$_{0.13}$Ni$_{0.87}$Se$_2$/Ti (1.62 V) [51], MoS$_2$@NiS (1.64 V) [52], and Ni$_3$S$_2$/Ni foam (1.76 V) [53] (Fig. S32). Additionally, after a 40000 s continuous operation at 1.58 V, as shown in Fig. 7b, the Co$_3$S$_4$@FNC-Co3 electrocatalyst shows an excellent durability with only a slight current degradation, demonstrating the potential application of Co$_3$S$_4$@FNC-Co3 in overall water splitting.

To study the role of defect-rich Co$_3$S$_4$ and porous carbon in Co$_3$S$_4$@FNC-Co3 catalyst toward OER and HER electrocatalysis, a control sample was prepared according to the same synthesis procedure as Co$_3$S$_4$@FNC-Co3 but without the addition of cobalt salt, and the resultant product is denoted as carbon-based material (CBM). As compared with the Co$_3$S$_4$@FNC-Co3 sample, CBM displays very poor electrocatalytic activities toward OER and HER (Fig. S33), signifying that Co$_3$S$_4$ nanoparticle is mainly responsible for the remarkable OER/HER electrocatalytic activities of Co$_3$S$_4$@FNC-Co3.

Regarding the porous carbon in Co$_3$S$_4$@FNC-Co3, it not only ensures the homogeneous distribution and effective confinement of Co$_3$S$_4$ nanoparticles (Fig. 2e), but also endows the electrocatalyst with a large specific surface area (Fig. 3e) and a hydrophilic surface due to the presence of abundant hydroxyl groups, which can maximize the exposure of active sites and promotes mass diffusion.

The excellent bifunctional electrocatalytic performance and stability of Co$_3$S$_4$@FNC-Co3 could be attributed to its unique structural merits. (i) The nonstoichiometric cobalt sulfide with mixed valences of Co^{2+} and Co^{3+} endows intrinsic high catalytic

Table 1
HER electrocatalytic parameters of various Co$_3$S$_4$@FNC samples.

Materials[a]	TOF [S^{-1}][b]	Tafel slope [mV decade^{-1}]	j_0 [mA cm^{-2}][c]	J [mA cm^{-2}][d]
Co$_3$S$_4$@FNC-Co1	0.0132	168	0.2282	4.75
Co$_3$S$_4$@FNC-Co2	0.03275	123	0.3839	14.08
Co$_3$S$_4$@FNC-Co3	0.04127	103	0.5136	21.24
Co$_3$S$_4$@FNC-Co4	0.00504	191	0.1110	3.07

[a] All the parameters were measured under the same conditions, i.e., catalyst loading of 0.404 mg cm^{-2} on glassy carbon electrode in 1.0 M KOH solution.
[b] TOFs were measured at η = 200 mV.
[c] Exchange current densities (j_0) were obtained from Tafel curves by using extrapolation methods.
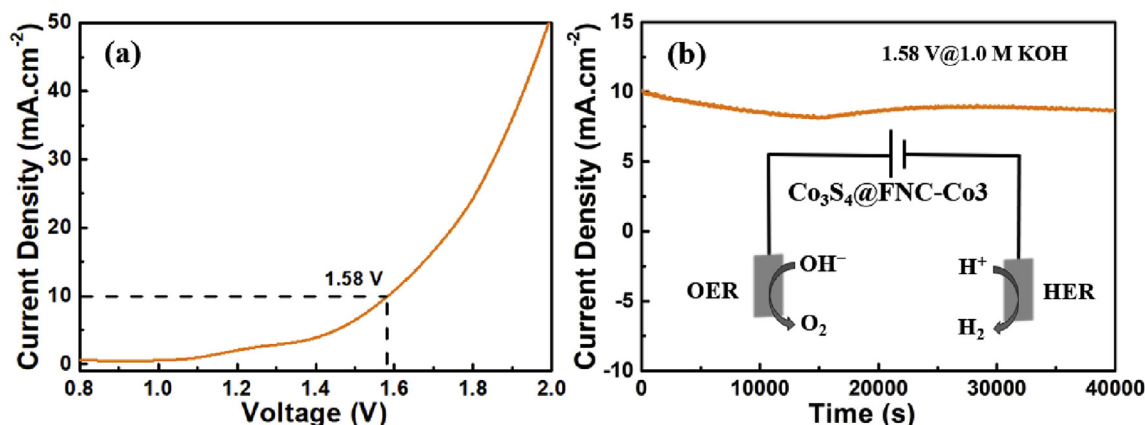[d] Cathodic current densities (j) were recorded at η = 200 mV.

Fig. 7. (a) LSV curves of Co$_3$S$_4$@FNC-Co3 as OER and HER bifunctional catalyst in 1.0 M KOH for overall water splitting, (b) the i—t tests of the Co$_3$S$_4$@FNC-Co3 on Ni foam electrolyzer at a voltage of 1.58 V. Inset to panel (b) is the illustration of the electrocatalytic reaction occurring on two electrodes. (A colour version of this figure can be viewed online.)

activities toward HER and OER. Importantly, Co^{3+} in Co$_3$S$_4$ would transform to CoOOH during OER catalysis (Fig. S23), and hence facilitate the absorption and deprotonation of oxygen-containing intermediate species (e.g., O$_{ad}$, OOH$_{ad}$) for O$_2$ production [54—56]. During OER process, the cobalt (oxy)hydroxide in-situ converted from the defect-rich Co$_3$S$_4$ nanoparticles may possess lattice-distortion structures [57] which can increase the number of grain boundaries of cobalt (oxy)hydroxide and hence expose more active sites to boost OER. In addition, the HER process in alkaline solution is almost dominated by the adsorption of H$_2$O molecules and the subsequent Volmer reaction [38,58]. Density-functional theory (DFT) calculations by Zhang et al. proved that sulfur vacancies in Co$_3$S$_4$ can not only improve the electronic conductivity, but also promote the adsorption of water molecules onto nearby Co atoms to lower the activation energy barrier of water molecule dissociation, which facilitates the formation of catalyst-H intermediats and finally boosts the HER electrocatalytic activity [37,55]. Density-functional theory (DFT) calculations by Zhang et al. proved that sulfur vacancies in Co$_3$S$_4$ can not only improve the electronic conductivity, but also promote the adsorption of water molecules onto nearby Co atoms to lower the activation energy barrier of water molecule dissociation, which facilitates the formation of catalyst-H intermediats and finally boosts the HER electrocatalytic activity. (ii) The presence of polar oxygen-/nitrogen-containing species on the carbon substrate of hierarchical Co$_3$S$_4$@FNC-Co3 microflower enables a hydrophilic surface, which is beneficial to the adsorption of correlated reaction species and hence promotes the corresponding reaction process [29]. (iii) The 3D microflower structure can effectively prevent the sheets from restacking/aggregating, which can not only sufficiently expose the catalytic active sites, but also facilitate the diffusion of both electrolyte and correlated intermediate species.

4. Conclusions

In summary, hierarchical carbon microflowers supporting sub-5 nm Co$_3$S$_4$ particles (Co$_3$S$_4$@FNC) were successfully prepared by a simple hydrothermal method via an unconventional vulcanization process, in which the strong ligand En and CH$_2$O serve as structure-directive agents for guiding the growth of spherical or 2D sheet-like architecture for the polymer precursor, respectively, while the co-ordinated segments of TU-Co^{2+}-En in polymer precursor can effectively impede the excessive growth of metal sulfide particles during hydrothermal processing. This unique structure such as defect and hierarchical porous texture helped the resultant

catalysts to maximize the exposure of active sites and facilitated the mass transfer for efficient OER and HER electrocatalysis, and the defect-rich Co$_3$S$_4$@FNC-Co3 sample was identified as the most active one among the series, showing an overpotential of only 250 mV and 140 mV to reach 10 mA cm^{-2} when catalyzing OER and HER in 1.0 M KOH aqueous solution, respectively. Furthermore, the remarkable operation stability of Co$_3$S$_4$@FNC-Co3 in OER and HER catalysis outperforms the state-of-the-art RuO$_2$ and commercial Pt/C catalysts. In particular, when Co$_3$S$_4$@FNC-Co3 was utilized as a bifunctional electrocatalyst in the cathode and anode of an alkaline water electrolyzer, a bias of only 1.580 V was able to implement a working current density of 10 mA cm^{-2}. The strategy in present work may be exploited for rational design and engineering of advanced multifunctional composites of nanostructured TMSs and carbons with hierarchical architectures for a wide range of electrochemical energy devices, such as fuel cells, supercapacitors, batteries, etc.

Declaration of competing interest

The authors of this paper declare that they have no financial, consultative, institutional, and other relationships that might lead to bias or conflict of interest.

CRediT authorship contribution statement

Xiaojing Zhu: Writing - original draft. **Jiale Dai:** Formal analysis. **Ligui Li:** Writing - review & editing. **Dengke Zhao:** Data curation. **Zexing Wu:** Resources. **Zhenghua Tang:** Resources. **Li-Jun Ma:** Resources. **Shaowei Chen:** Writing - review & editing.

Acknowledgements

Appendix A. Supplementary data

Supplementary data to this article can be found online at

References

[1] D. Deng, K.S. Novoselov, Q. Fu, N. Zheng, Z. Tian, X. Bao, Catalysis with two-dimensional materials and their heterostructures, Nat. Nanotechnol. 11 (2016) 218.

[2] J. Wu, L. Hu, N. Wang, Y. Li, D. Zhao, L. Li, X. Peng, Z. Cui, L.-J. Ma, Y. Tian, X. Wang, Surface confinement assisted synthesis of nitrogen-rich hollow carbon cages with Co nanoparticles as breathable electrodes for Zn-air batteries, Appl. Catal. B Environ. 254 (2019) 55—65.

[3] M. Gong, Z. Deng, D. Xiao, L. Han, T. Zhao, Y. Lu, T. Shen, X. Liu, R. Lin, T. Huang, G. Zhou, H. Xin, D. Wang, One-nanometer-thick Pt₃Ni bimetallic alloy nanowires advanced oxygen reduction reaction: integrating multiple advantages into one catalyst, ACS Catal. 9 (5) (2019) 4488—4494.

[4] J.-Y. Zhang, H. Wang, Y. Tian, Y. Yan, Q. Xue, T. He, H. Liu, C. Wang, Y. Chen, B.Y. Xia, Anodic hydrazine oxidation assists energy-efficient hydrogen evolution over a bifunctional cobalt perselenide nanosheet electrode, Angew. Chem. Int. Ed. 57 (26) (2018) 7649—7653.

[5] X. Peng, L. Zhang, Z. Chen, L. Zhong, D. Zhao, X. Chi, X. Zhao, L. Li, X. Lu, K. Leng, C. Liu, W. Liu, W. Tang, K.P. Loh, Hierarchically porous carbon plates derived from wood as bifunctional ORR/OER electrodes, Adv. Mater. 31 (16) (2019) 1900341.

[6] I.S. Amiinu, Z. Pu, X. Liu, K.A. Owusu, H.G.R. Monestel, F.O. Boakye, H. Zhang, S. Mu, Multifunctional Mo—N/C@MoS₂ electrocatalysts for HER, OER, ORR, and Zn—air batteries, Adv. Funct. Mater. 27 (44) (2017) 1702300.

[7] Y. Zhao, X. Zhang, X. Jia, G.I.N. Waterhouse, R. Shi, X. Zhang, F. Zhan, Y. Tao, L.-Z. Wu, C.-H. Tung, D. O'Hare, T. Zhang, Sub-3 nm ultrafine monolayer layered double hydroxide nanosheets for electrochemical water oxidation, Adv. Energy Mater. 8 (18) (2018) 1703585.

[8] Z. Wang, H. Liu, R. Ge, X. Ren, J. Ren, D. Yang, L. Zhang, X. Sun, Phosphorus-doped Co₃O₄ nanowire array: a highly efficient bifunctional electrocatalyst for overall water splitting, ACS Catal. 8 (3) (2018) 2236—2241.

[9] Y. Li, F.-M. Li, X.-Y. Meng, S.-N. Li, J.-H. Zeng, Y. Chen, Ultrathin Co₃O₄ nanomeshes for the oxygen evolution reaction, ACS Catal. 8 (3) (2018) 1913—1920.

[10] D. Zhang, H. Mou, F. Lu, C. Song, D. Wang, A novel strategy for 2D/2D NiS/graphene heterostructures as efficient bifunctional electrocatalysts for overall water splitting, Appl. Catal. B Environ. 254 (2019) 471—478.

[11] I.S. Amiinu, Z. Pu, D. He, H.G.R. Monestel, S. Mu, Scalable cellulose-sponsored functionalized carbon nanorods induced by cobalt for efficient overall water splitting, Carbon 137 (2018) 274—281.

[12] P. Wang, H. He, Z. Pu, L. Chen, C. Zhang, Z. Wang, S. Mu, Phosphorization engineering ameliorated the electrocatalytic activity for overall water splitting on Ni₃S₂ nanosheets, Dalton Trans. 48 (35) (2019) 13466—13471.

[13] N. Wang, L. Li, D. Zhao, X. Kang, Z. Tang, S. Chen, Graphene composites with cobalt sulfide: efficient trifunctional electrocatalysts for oxygen reversible catalysis and hydrogen production in the same electrolyte, Small 13 (33) (2017) 1701025.

[14] P. Chen, T. Zhou, M. Zhang, Y. Tong, C. Zhong, N. Zhang, L. Zhang, C. Wu, Y. Xie, 3D nitrogen-anion-decorated nickel sulfides for highly efficient overall water splitting, Adv. Mater. 29 (30) (2017) 1701584.

[15] Z. Wu, X. Wang, J. Huang, F. Gao, A Co-doped Ni—Fe mixed oxide mesoporous nanosheet array with low overpotential and high stability towards overall water splitting, J. Mater. Chem. 6 (1) (2018) 167—178.

[16] S. Anantharaj, S.R. Ede, K. Sakthikumar, K. Karthick, S. Mishra, S. Kundu, Recent trends and perspectives in electrochemical water splitting with an emphasis on sulfide, selenide, and phosphide catalysts of Fe, Co, and Ni: a review, ACS Catal. 6 (12) (2016) 8069—8097.

[17] J. Yu, G. Cheng, W. Luo, Ternary nickel—iron sulfide microflowers as a robust electrocatalyst for bifunctional water splitting, J. Mater. Chem. 5 (30) (2017) 15838—15844.

[18] G. Fu, J.-M. Lee, Ternary metal sulfides for electrocatalytic energy conversion, J. Mater. Chem. 7 (16) (2019) 9386—9405.

[19] Y.P. Zhu, T.Y. Ma, M. Jaroniec, S.Z. Qiao, Self-templating synthesis of hollow Co₃O₄ microtube Arrays for highly efficient water electrolysis, Angew. Chem. Int. Ed. 56 (5) (2017) 1324—1328.

[20] J. Bai, B. Xi, H. Mao, Y. Lin, X. Ma, J. Feng, S. Xiong, One-step construction of N,P-codoped porous carbon sheets/CoP hybrids with enhanced lithium and potassium storage, Adv. Mater. 30 (35) (2018) 1802310.

[21] H.-F. Wang, C. Tang, B. Wang, B.-Q. Li, Q. Zhang, Bifunctional transition metal hydroxysulfides: room-temperature sulfurization and their applications in Zn—air batteries, Adv. Mater. 29 (35) (2017) 1702547.

[22] Z.-Q. Liu, H. Cheng, N. Li, T.Y. Ma, Y.-Z. Su, ZnCo₂O₄ quantum dots anchored on nitrogen-doped carbon nanotubes as reversible oxygen reduction/evolution electrocatalysts, Adv. Mater. 28 (19) (2016) 3777—3784.

[23] P. Ganesan, M. Prabu, J. Sanetuntikul, S. Shanmugam, Cobalt sulfide nanoparticles grown on nitrogen and sulfur codoped graphene oxide: an efficient electrocatalyst for oxygen reduction and evolution reactions, ACS Catal. 5 (6) (2015) 3625—3637.

[24] Q. Yun, Q. Lu, X. Zhang, C. Tan, H. Zhang, Three-Dimensional architectures constructed from transition-metal dichalcogenide nanomaterials for electrochemical energy storage and conversion, Angew. Chem. Int. Ed. 57 (3) (2018) 626—646.

[25] X. Zuo, K. Chang, J. Zhao, Z. Xie, H. Tang, B. Li, Z. Chang, Bubble-template-assisted synthesis of hollow fullerene-like MoS₂ nanocages as a lithium ion battery anode material, J. Mater. Chem. 4 (1) (2016) 51—58.

[26] K. Cho, S.-H. Han, M.P. Suh, Copper—organic framework fabricated with CuS nanoparticles: synthesis, electrical conductivity, and electrocatalytic activities for oxygen reduction reaction, Angew. Chem. Int. Ed. 55 (49) (2016) 15301—15305.

[27] J.A. García-Valenzuela, Simple thiourea hydrolysis or intermediate complex mechanism? Taking up the formation of metal sulfides from metal—thiourea alkaline solutions, Comments Inorg. Chem. 37 (2) (2017) 99—115.

[28] J. Park, A.C. Hinckley, Z. Huang, D. Feng, A.A. Yakovenko, M. Lee, S. Chen, X. Zou, Z. Bao, Synthetic routes for a 2D semiconductive copper hexahydroxybenzene metal—organic framework, J. Am. Chem. Soc. 140 (44) (2018) 14533—14537.

[29] J. Chen, P. Cui, G. Zhao, K. Rui, M. Lao, Y. Chen, X. Zheng, Y. Jiang, H. Pan, S.X. Dou, W. Sun, Low-coordinate iridium oxide confined on graphitic carbon nitride for highly efficient oxygen evolution, Angew. Chem. Int. Ed. 58 (36) (2019) 12540—12544.

[30] F. Luo, D. Ma, Y. Li, H. Mi, P. Zhang, S. Luo, Hollow Co₃S₄/C anchored on nitrogen-doped carbon nanofibers as a free-standing anode for high-performance Li-ion batteries, Electrochim. Acta 299 (2019) 173—181.

[31] W. Niu, Z. Li, K. Marcus, L. Zhou, Y. Li, R. Ye, K. Liang, Y. Yang, Composite materials: surface-modified porous carbon nitride composites as highly efficient electrocatalyst for Zn-air batteries, Adv. Energy Mater. 8 (1) (2018) 1870002.

[32] J. Xie, H. Zhang, S. Li, R. Wang, X. Sun, M. Zhou, J. Zhou, X.W. Lou, Y. Xie, Defect-rich MoS₂ ultrathin nanosheets with additional active edge sites for enhanced electrocatalytic hydrogen evolution, Adv. Mater. 25 (40) (2013) 5807—5813.

[33] Z. Li, Y. Zhang, Y. Feng, C.-Q. Cheng, K.-W. Qiu, C.-K. Dong, H. Liu, X.-W. Du, Co₃O₄ nanoparticles with ultrasmall size and abundant oxygen vacancies for boosting oxygen involved reactions, Adv. Funct. Mater. 29 (36) (2019) 1903444.

[34] Y. Zhu, H.A. Tahini, Y. Wang, Q. Lin, Y. Liang, C.M. Doherty, Y. Liu, X. Li, J. Lu, S.C. Smith, C. Selomulya, X. Zhang, Z. Shao, H. Wang, Pyrite-type ruthenium disulfide with tunable disorder and defects enables ultra-efficient overall water splitting, J. Mater. Chem. 7 (23) (2019) 14222—14232.

[35] M. Zheng, Y. Ding, L. Yu, X. Du, Y. Zhao, In situ grown pristine cobalt sulfide as bifunctional photocatalyst for hydrogen and oxygen evolution, Adv. Funct. Mater. 27 (11) (2017) 1605846.

[36] L. Yu, L. Zhang, H.B. Wu, X.W. Lou, formation of NiₓCo₃₋ₓS4 hollow nanoprisms with enhanced pseudocapacitive properties, Angew. Chem. Int. Ed. 53 (14) (2014) 3711—3714.

[37] C. Zhang, Y. Shi, Y. Yu, Y. Du, B. Zhang, Engineering sulfur defects, atomic thickness, and porous structures into cobalt sulfide nanosheets for efficient electrocatalytic alkaline hydrogen evolution, ACS Catal. 8 (9) (2018) 8077—8083.

[38] J. Zhang, W. Xiao, P. Xi, S. Xi, Y. Du, D. Gao, J. Ding, Activating and optimizing activity of CoS2 for hydrogen evolution reaction through the synergic effect of N dopants and S vacancies, ACS Energy Lett. 2 (5) (2017) 1022—1028.

[39] X. Zhu, J. Chong, T. Hu, X. Wang, Y. Tian, Enhanced stability and metallic modification of polymeric and carbonaceous nanospheres through precursor engineering via a one-pot aqueous strategy assisted by iron ions, J. Mater. Chem. 5 (18) (2017) 8297—8306.

[40] X. Zhu, S. Wang, W. Huang, Y. Tian, X. Wang, Controllable synthesis of mesoporous carbon nanospheres with uniform size by a facile one-pot aqueous strategy under highly acidic conditions, Carbon 105 (2016) 521—528.

[41] J. Chen, H. Zhang, P. Liu, Y. Li, G. Li, T. An, H. Zhao, Thiourea sole doping reagent approach for controllable N, S co-doping of pre-synthesized large-sized carbon nanospheres as electrocatalyst for oxygen reduction reaction, Carbon 92 (2015) 339—347.

[42] W. Niu, L. Li, X. Liu, N. Wang, J. Liu, W. Zhou, Z. Tang, S. Chen, Mesoporous N-doped carbons prepared with thermally removable nanoparticle templates: an efficient electrocatalyst for oxygen reduction reaction, J. Am. Chem. Soc. 137 (16) (2015) 5555—5562.

[43] W. Li, X. Gao, D. Xiong, F. Wei, W.-G. Song, J. Xu, L. Liu, Hydrothermal synthesis of monolithic Co₃Se₄ nanowire electrodes for oxygen evolution and overall water splitting with high efficiency and extraordinary catalytic stability, Adv. Energy Mater. 7 (17) (2017) 1602579.

[44] N. Weidler, S. Paulus, J. Schuch, J. Klett, S. Hoch, P. Stenner, A. Maljusch, J. Brötz, C. Wittich, B. Kaiser, W. Jaegermann, CoOₓ thin film deposited by CVD as efficient water oxidation catalyst: change of oxidation state in XPS and its correlation to electrochemical activity, Phys. Chem. Chem. Phys. 18 (16) (2016) 10708—10718.

[45] A. Sivanantham, P. Ganesan, S. Shanmugam, Hierarchical NiCo₂S₄ nanowire arrays supported on Ni foam: an efficient and durable bifunctional electrocatalyst for oxygen and hydrogen evolution reactions, Adv. Funct. Mater. 26 (26) (2016) 4661—4672.

[46] Y. Xue, Z. Zuo, Y. Li, H. Liu, Y. Li, Graphdiyne-supported NiCo₂S₄ nanowires: a highly active and stable 3D bifunctional electrode material, Small 13 (31) (2017) 1700936.

[47] X. Xu, F. Song, X. Hu, A nickel iron diselenide-derived efficient oxygen-evolution catalyst, Nat. Commun. 7 (2016) 12324.

[48] J. Masa, P. Weide, D. Peeters, I. Sinev, W. Xia, Z. Sun, C. Somsen, M. Muhler, W. Schuhmann, Amorphous cobalt boride (Co₂B) as a highly efficient non-precious catalyst for electrochemical water splitting: oxygen and hydrogen

evolution, Adv. Energy Mater. 6 (6) (2016) 1502313.

[49] Y. Guo, J. Tang, Z. Wang, Y.-M. Kang, Y. Bando, Y. Yamauchi, Elaborately assembled core-shell structured metal sulfides as a bifunctional catalyst for highly efficient electrochemical overall water splitting, Nano Energy 47 (2018) 494–502.

[50] Y. Xu, W. Tu, B. Zhang, S. Yin, Y. Huang, M. Kraft, R. Xu, Nickel nanoparticles encapsulated in few-layer nitrogen-doped graphene derived from metal–organic frameworks as efficient bifunctional electrocatalysts for overall water splitting, Adv. Mater. 29 (11) (2017) 1605957.

[51] T. Liu, A.M. Asiri, X. Sun, Electrodeposited Co-doped NiSe₂ nanoparticles film: a good electrocatalyst for efficient water splitting, Nanoscale 8 (7) (2016) 3911–3915.

[52] Q. Qin, L. Chen, T. Wei, X. Liu, MoS₂/NiS yolk–shell microsphere-based electrodes for overall water splitting and asymmetric supercapacitor, Small 15 (29) (2019) 1803639.

[53] L.-L. Feng, G. Yu, Y. Wu, G.-D. Li, H. Li, Y. Sun, T. Asefa, W. Chen, X. Zou, High-index faceted Ni₃S₂ nanosheet arrays as highly active and ultrastable electrocatalysts for water splitting, J. Am. Chem. Soc. 137 (44) (2015) 14023–14026.

[54] L. Liang, H. Cheng, F. Lei, J. Han, S. Gao, C. Wang, Y. Sun, S. Qamar, S. Wei, Y. Xie, Metallic single-unit-cell orthorhombic cobalt diselenide atomic layers: robust water-electrolysis catalysts, Angew. Chem. Int. Ed. 54 (41) (2015) 12004–12008.

[55] H. Xu, J. Cao, C. Shan, B. Wang, P. Xi, W. Liu, Y. Tang, MOF-derived hollow CoS decorated with CeOₓ nanoparticles for boosting oxygen evolution reaction electrocatalysis, Angew. Chem. Int. Ed. 57 (28) (2018) 8654–8658.

[56] J. Dai, D. Zhao, W. Sun, X. Zhu, L.-J. Ma, Z. Wu, C. Yang, Z. Cui, L. Li, S. Chen, Cu(II) ions induced structural transformation of cobalt selenides for remarkable enhancement in oxygen/hydrogen electrocatalysis, ACS Catal. 9 (12) (2019) 10761–10772.

[57] G. Huang, Z. Xiao, R. Chen, S. Wang, Defect engineering of cobalt-based materials for electrocatalytic water splitting, ACS Sustain. Chem. Eng. 6 (12) (2018) 15954–15969.

[58] B. Lu, L. Guo, F. Wu, Y. Peng, J.E. Lu, T.J. Smart, N. Wang, Y.Z. Finfrock, D. Morris, P. Zhang, N. Li, P. Gao, Y. Ping, S. Chen, Ruthenium atomically dispersed in carbon outperforms platinum toward hydrogen evolution in alkaline media, Nat. Commun. 10 (1) (2019) 631.